Insight into bulk charge transfer of lithium metal anodes by synergism of nickel seeding and LiF-Li$_3$N-Li$_2$S co-doped interphase

Zhendong Li [a], Liyuan Huai [a], Shun Li [a], Mingming Ma [a], Kailin Luo [a], Yang Zhao [b], Deyu Wang [a,c,d,*], Xueliang Sun [b,*], Zhe Peng [a,*]

[a] Ningbo Institute of Materials Technology and Engineering, Chinese Academy of Sciences, Ningbo 315201, China
[b] Department of Mechanical and Materials Engineering, University of Western Ontario, London ON N6A 5B9, Canada
[c] Key Laboratory of Optoelectronic Chemical Materials and Devices, School of Chemical and Environmental Engineering, Jianghan University, Wuhan 430056, China
[d] Tianmu Lake Institute of Advanced Energy Storage Technologies, Liyang 213300, China

ABSTRACT

Cycling lithium (Li) metal anode with a low negative/positive capacity (N/P) ratio is critical to build high-energy-density Li metal batteries (LMBs). Many strategies focusing on interfacial protection are limited to shallow conditions using excessive Li with a high negative/positive capacity (N/P) ratio > 50. Herein, we demonstrate a deeply enhanced charge transfer kinetic by a rational incorporation of nickel (Ni) seeds in the Li anodes with a tailored interfacial chemistry. The Ni seeds in the bulk Li anode not only act as well-dispersed nucleation sites to enable Ni-seeded growth of granular Li deposits, but also adsorb acetonitrile (AN) molecules when the Ni-seeded Li anodes are paired with an AN-based electrolyte using lithium bis-(fluorosulfonyl)imide as salt, forming a fast Li$^+$ conducting interphase with co-produced LiF, Li$_3$N and Li$_2$S components. These benefits conduct an exchange current density ∼ 20 times higher than that of the bare Li in conventional carbonate electrolytes. Stable cycling of LMBs with a practical cathode loading (∼ 5 mAh cm^{-2}) and a low N/P capacity ratio of 2 is also demonstrated, showing the prominence of this remedy for developing high-energy-density LMBs.

1. Introduction

Surging demands of high-energy-density storage systems for electric vehicles and large power supply equipment constantly motivate the technology development beyond Li-ion chemistry [1,2], whereas the rechargeable batteries using ultralight and high energy-dense Li metal anodes have become the research focus during the past decades [3,4]. One of the most important features of Li metal anode is to break the intrinsic link between capacity and crystal structure of the host materials like graphite, leading to a "hostless" material of which the capacity is not stemmed from the host's existing crystal structure [5,6]. However, unlike the graphite with only ∼10% volume expansion between the fully lithiated and delithiated states (and limited capacity of 372 mAh g^{-1}) [5], the "hostless" Li metal anodes are always suffering from the infinite volume change, along with the non-uniform Li deposition in dendritic or mossy shapes, causing unstable solid-electrolyte interphase (SEI) and continuous consumption of electrolytes and Li metal during cycling [7]. The as-induced limited lifespan and safety concerns seriously impede the implementation of Li metal batteries (LMBs).

Various emerging strategies have been devoted to stabilizing Li/electrolyte interfaces, including electrolyte optimization [8–11], electrolyte solidification [12], and artificial protective layer construction [13–16]. Hosting Li metal into 3D structures is another important method to inhibit the excessive volume expansion of Li metal anodes [17–21]. Although stable and long cycling performances of Li metal anodes have been reported, most of them are conducted in a cell configuration with excessive Li anode. When designing high-energy-density LMBs, the cell components need to be rationally balanced, whereas the cathode area capacity and the negative/positive capacity ratio (N/P ratio) are two of the most important cell parameters. For a typical coin cell from the state-of-the-art, the cathode area capacity is usually around 1 mAh cm^{-2} or even lower, while thick Li metal anodes with a thickness of 250 μm or thicker are often used, generally resulting in a high N/P ratio > 50 and hundreds of stable cycles (Fig. 1a). However, cycling with excessive Li often cover unexpected minor defects which could exaggerate in lean Li conditions, and any parasites such as Li dendrites and side reactions will engender serious cell polarization and capacity fading (Fig. 1b) [22]. Although the scientific community has come into consideration of addressing the Li metal cyclability in realistic LMB configurations [22–25], developing an efficient method to protect Li metal in practical conditions with high-loading and low N/P ratio still possesses high priorities.
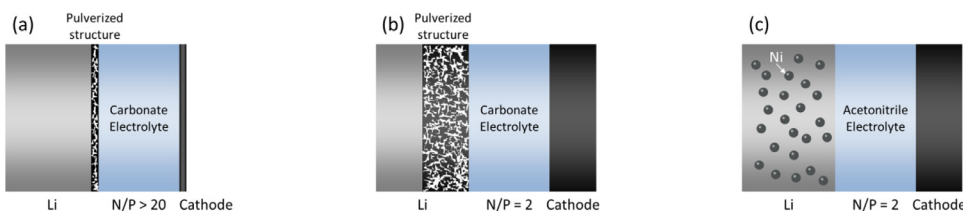
Fig. 1. Schematic representations of inner structures of LMBs with (a) bare Li anode, carbonate electrolyte and a N/P ratio > 20, (b) bare Li anode, carbonate electrolyte and a N/P ratio =2 and (c) Ni seeded Li anode, acetonitrile electrolyte and a N/P ratio = 2.

In this work, we investigate the remedy to enable stable cycling of LMBs with a practical cathode loading of 5 mAh cm^{-2} at a low N/P ratio of 2, based on a deeply improved bulk charge transfer of Li metal anodes. The latter is achieved by synergism of suitable metal seeding and tailored interfacial chemistry. A key issue inherent to stable Li cycling at low N/P ratio is poor uniformity of Li plating/stripping at high depth of discharge (DOD), which is generally not considered in excessive Li conditions. Herein, we find that Ni seeds in the bulk Li anode not only provided high binding energy with Li atoms and acted as the well-dispersed nucleation sites to enable Ni-seeded growth of granular Li deposits, but also enabled the formation of a fast Li$^+$ conducting LiF-Li$_3$N-Li$_2$S co-doped interphase when deeply cycling with an acetonitrile-based electrolyte. Based on these benefits, LMBs with a high cathode loading (~ 5 mAh cm^{-2}) and a low N/P capacity ratio of 2 can achieve > 160 stable cycles, and proof-of-concept high-energy-density LMBs (> 350 Wh kg^{-1}) with a stable cycling over 100 cycles were further demonstrated (Fig. 1c).

2. Results and discussion

2.1. Ni seeding to tailor Li deposition

The uniformly dispersed Ni seeds in Li electrodes were obtained via precipitation process of Ni in Li during the reaction of Ni oxide with molten Li. Core-shell Ni-Ni oxide structures were easily generated via the thermal treatment of Ni foams (NFs) in air conditions. Three samples, bare NF, NF treated at 400 and 500 °C were compared and denoted as NF, NF400 and NF500, respectively. As shown in Fig. S1a, apparent color changes clearly indicate the different oxidization degrees of NFs with increasing the treatment temperatures. A well-defined NiO peak was only observed on the X-ray diffraction (XRD) pattern of NF500 (Fig. S1b), which exhibits sharply changed surface morphology and chemistry compared to those of NF (Fig. S1c-S1f). To demonstrate the unique advantage of Ni seeding, the Cu oxides which only generated large Cu clusters posterior to the reaction with molten Li were also compared. Previously, the Cu oxides have been proved as efficacious lithiophilic materials, and applied on various host structures to form composite Li electrodes through hydrothermal or electrochemical deposition techniques [26–28]. In this work, Cu foams (CF) were heated in air conditions at 200 and 300 °C (denoted as CF200 and CF300, respectively) to achieve surface oxidations, as shown in Fig. S2a and S2b, with significantly changed surface morphology and chemistry of CF300 compared to those of CF (Fig. S2c-S2f).

Although the oxidation temperatures are different for NF and CF, they obeyed a general trend, i.e. the molten Li uptake rate is directly depending on the surface oxidization degree of the substrates, as demonstrated by the monitored Li uptakes on NF400 and NF500 (Fig. S1g and S1h), or on CF200 and CF300 (Fig. S2g and S2h). It should be mentioned that excessive thermal treatments (longer treatment time or higher treatment temperature) would lead to over-oxidation of NF or CF, getting easily fire during the molten Li infusion process. Thus, later studies were carried out on NF500 and CF300 obtained at the optimal conditions, whereas first attention was paid on the much faster molten Li uptake in NF500 than CF300 (Fig. 2b), for which quantified Li uptake values were calculated by the ratio of Li uptake area on the total area of the substrate by the pixel counting of the converted black and white binary

images (Fig. 2a and S3, with detailed calculations provided in the supporting information). It can be seen that NF500 achieved a Li uptake > 80% in less than 10 s, only in half the time of the case of CF300. One possible reason for the latter observation is the higher binding energy of Li atom on Ni surface than that on the Cu surface (Fig. 2c), promoting fast Li adsorption and infusion after the initial generation of Ni seeds in the composite electrode.

A similar thickness of 400 μm was observed for CF300@Li and NF500@Li electrodes (Fig. 2d and e, respectively), with infused Li through the inner pores of the skeletons (Fig. S4). However, significantly different structural morphologies were observed between these electrodes, i.e. Clear filament-like clusters were observed on the surface of CF300@Li electrode (Figs. 2d and S5a), while tremendous nanoparticles were uniformly seeded in the electrode of NF500@Li (Figs. 2e and S5b). Such a structural difference could also be observed inside the composite electrodes, as shown in the cross-sectional scanning electron microscope (SEM) images (Figs. S5c and S5d). According to the energy dispersive spectrometer (EDS) mapping, the Cu mapping and the clusters formed on the surface of CF300@Li highly overlapped (Fig. S6), confirming the formations of the heterogeneous Cu clusters on CF300@Li. Furthermore, the SEM and EDS images of the sub-surfaces of CF300@Li and NF500@Li after a Li stripping of 0.5 mAh cm^{-2} were also measured. As shown in Fig. S7a, uneven distributions of Cu and O signals were observed for CF300@Li, indicating the formations of heterogeneous Cu clusters and by-produced Li$_2$O in the bulk structure of CF300@Li. In contrast, even distributions of Ni and O elements on the sub-surfaces of NF500@Li demonstrate the uniformity of the Ni seeded Li structure (Fig. S7b). The Ar$^+$-etching assisted X-ray photoelectron spectroscopy (XPS) measurements show exact Cu metal ($\triangle_{metal}$ = 19.8 eV between Cu 2p$_{1/2}$ and Cu 2p$_{2/3}$, Fig. 2f) and Ni metal ($\triangle_{metal}$ = 17.3 eV between Ni 2p$_{1/2}$ and Ni 2p$_{2/3}$, Fig. 2g) signals in depths of CF300@Li and NF500@Li, respectively, demonstrating the occupation of Cu or Ni precipitates in the whole composite electrodes. The byproduct Li$_2$O could also be observed in depths of these two samples (Fig. S8) [29], certifying that the Cu and Ni precipitates were produced from the reactions of their oxides with molten Li (M$_x$O + 2Li → Li$_2$O + xM). Based on these results, it can be presumed that the special morphologies observed on CF300@Li and NF500@Li should arise from the different precipitation kinetics of Cu and Ni in molten Li. According to the Cu-Li and Ni-Li binary phase diagrams (Fig. 2h) [30], no hypoeutectic alloy exists for these two systems, showing negligible solubility of Cu or Ni in molten Li. The unique crystal transition isotherm at ~ 181 °C on Ni-Li diagram suggests the monotone precipitation of Ni seeds during the cooling-down process of molten Li (molten Li infusion operated at 250 °C), however, the formation of large Cu clusters is possible in case of heterogeneous precipitation during the cooling-down process, as shown in the low Li content region. These considerations are consistent with the observed morphologies of CF300@Li and NF500@Li electrodes.

Electrochemical reductions (0 V vs. Li/Li$^+$) of surface oxides on CF300 and NF500 into metal precipitates and Li$_2$O were also performed without the presence of Li metal (Fig. S9). As shown in Fig. 2i, large clusters were generated on the reduced CF300, while more refined small agglomerates were formed on the reduced NF500. These reduced scaffolds were then subject to cycling Li CE test using carbonate-based electrolyte (denoted as C-ELY, with the constitution of 1 M LiPF$_6$ in ethylene carbonate (EC): diethyl carbonate (DEC) (1:1 by vol.) + 5 vol% fluo-
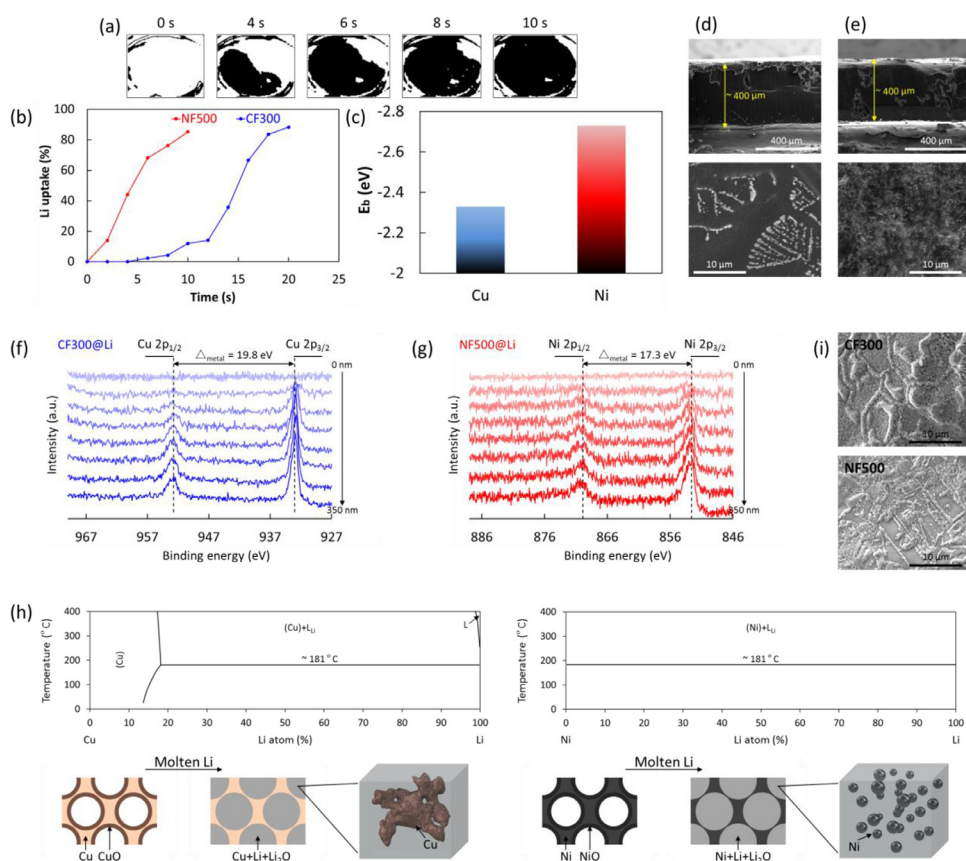
Fig. 2. (a) Converted binary images of molten Li infusion into NF500; (b) Molten Li uptake rates of CF300 and NF500; (c) Binding energies of Li atoms on Cu(100) and Ni(100) surfaces; (d, e) SEM images of (d) CF300@Li and (e) NF500@Li electrodes; (f, g) Ar⁺-etching assisted XPS analysis for (f) Cu 2p spectra of CF300@Li electrode and (g) Ni 2p spectra of NF500@Li electrode; (h) Cu-Li and Ni-Li phase diagrams and schematic representations of CF300@Li and NF500@Li electrodes [30]; (i) Reduced surface morphologies of CF300 and NF500.

roethylene carbonate (FEC)), whereas smaller Li nucleation overpotential (Fig. S10) with more stable performance (Fig. S11b) was achieved for the reduced NF500. The smaller Li nucleation overpotential on the reduced NF500 is consistent with the higher binding energy of Li atom on Ni surface than that on Cu (Fig. 2c). It should be mentioned that similar and poor performances were obtained on the bare CF and NF (Fig. S11a), indicating that the skeletons of these foams have little impact on the stability of Li metal anode, and the improved performances of Li plating/stripping on NF500 should arise from the Ni seeded bulk Li structure. As well, the voltage profiles recorded from the symmetrical cells also showed much more stable polarization for the cell using NF500@Li electrodes (Fig. S11c), which exhibited 2.5 times longer lifespan (∼ 3000 h) and 3 times lower polarization (∼ 14 mV) than those obtained for the cell using CF300@Li electrodes (∼ 1250 h and 47 mV). The surface morphologies of the cycled CF300@Li or NF500@Li electrodes after a cycling time of 200 h of the symmetrical cells are shown in Fig. S11d. The cycled NF500@Li electrode still maintained a relatively compact surface, while the surface of the cycled CF300@Li electrode was highly pulverized. These results jointly indicate much more stable Li plating/stripping behaviors in the presence of Ni seeds, compared to those with Cu clusters.

To clarify the bulk Li plating/stripping behaviors in CF300@Li and NF500@Li, various sequences were applied in C-ELY by first stripping 8 mAh cm⁻² Li from the electrodes (state S8), then progressively plating-back Li of 2 mAh cm⁻² (state S8-P2), 4 mAh cm⁻² (state S8-P4) and 8 mAh cm⁻² (state S8-P8), performed at a current density of 0.5 mA cm⁻². As shown in Fig. 3a, grave roughness was produced on the surface of bare Li at the state S8. It should be mentioned that stripping 8 mAh cm⁻² Li only represents a DOD of 10% of the Li foil (∼ 65 mAh cm⁻²), while the surface heterogeneity caused by the uneven bulk charge transfer is already significant. These hazardous existences further act as "hot spots" to seriously affect further Li plating uniformity, as shown by the

largely generated dendritic deposits by the increase of Li plating capacity. These features will even be aggravated at high DODs of Li metal anodes, typically rooted in the conditions of low N/P ratio. Interestingly, for the CF300@Li electrode, large Cu clusters were observed at the state S8, which seem to beneficially enhance the subsequent Li nucleation and deposition, as shown by the noodle-like deposits formed at the states of S8-P2 and S8-P4 (Fig. 3b). However, by further increasing the Li plating capacity to the state S8-P8, dendrites were still formed at the crevices between the adjacent noodle-like deposits, indicating that the large Cu clusters are not able to impact the Li deposition while the latter occurs at inaccessible spaces by the Cu clusters. In contrast, due to the uniformly dispersed Ni seeds in the bulk structure, uniform Li depositions were achieved on NF500@Li, with well-seeded growth of granular deposits that progressively merged to form a compact Li layer up to the state S8-P8 (Fig. 3c). An overview of the Li plating/stripping behaviors on the investigated samples in C-ELY is shown in Fig. 3d, among which the much improved bulk charge transfer in the Ni-seeded structure is illustrated.

As above-demonstrated, the formations of large Cu clusters arising from the heterogeneous precipitation with molten Li affected the bulk charge transfer of Li metal anodes. In the case of highly lithiophilic materials (such as Ag, Zn, etc.) with high solid solubility with Li, the formations of hetero-metal clusters would be further favored, and the additional alloying/dealloying processes might also retard the bulk transfer of Li metal anodes. To demonstrate the latter issue, we have prepared Li composite anodes based on ZnO coated Ni foams (denoted as (Ni+ZnO)@Li), and compared with NF500@Li (which corresponds to (Ni+NiO@Li)). The ZnO coated Ni foams were fabricated using a previously reported method [31]. Consistent Zn and O elemental mapping (Fig. S12a) and a typical interpeak distance of 23.1 eV between the Zn 2p₃/₂ and Zn 2p₁/₂ doublet (Fig. S12b) demonstrate the successful ZnO coating on the Ni foams [32]. Due to the lithiophilic ZnO coating, the
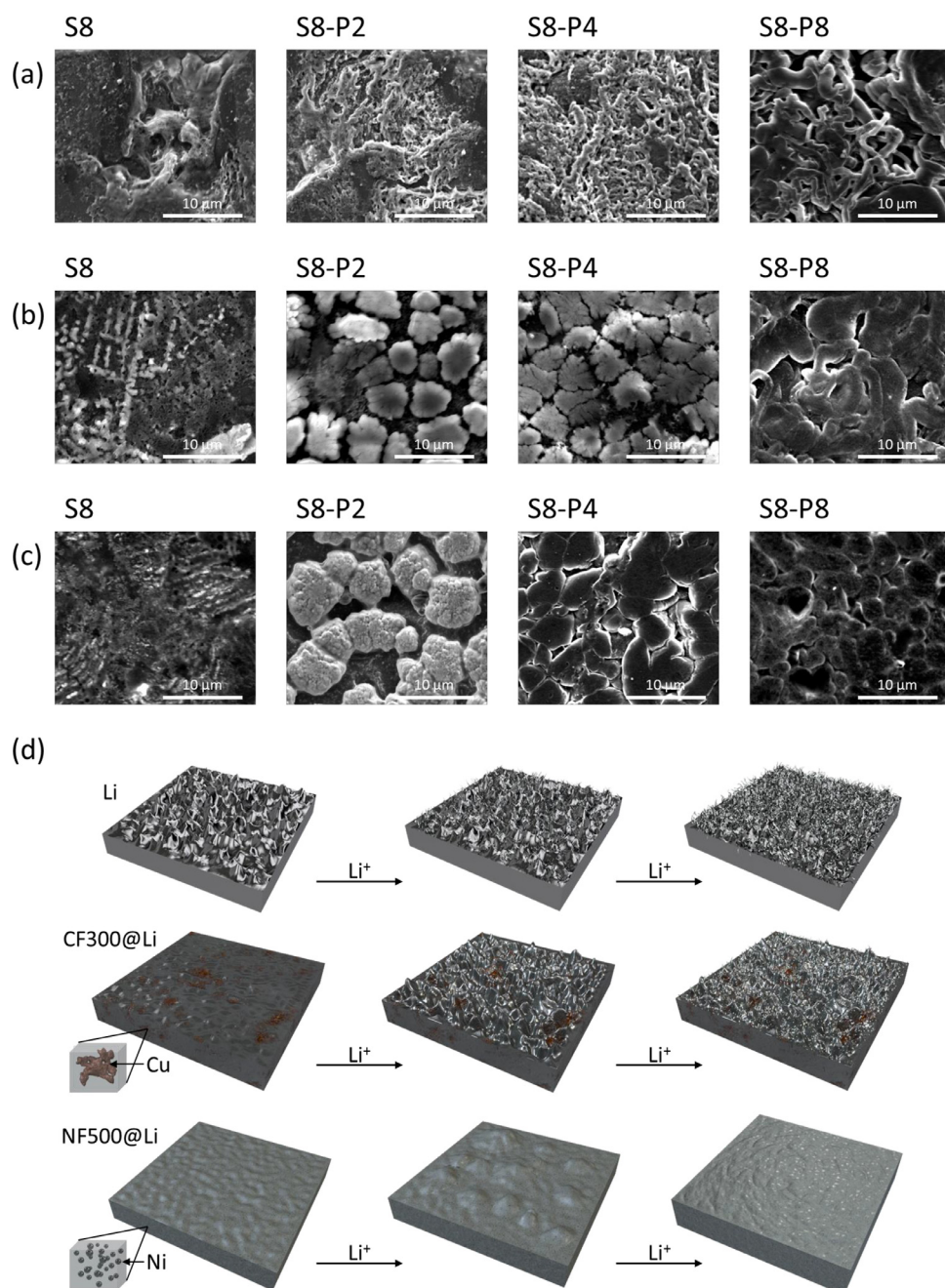
Fig. 3. Morphologies of (a) bare Li, (b) CF300@Li and (c) NF500@Li electrodes following various Li plating/stripping sequences in C-ELY; (d) Schematic representations of Li plating-back behaviors on bare Li, CF300@Li and NF500@Li electrodes in C-ELY.

(Ni+ZnO)@Li composite electrode could be easily obtained by infusing molten Li (Fig. S12c). As expected, even more clusters were formed on (Ni+ZnO)@Li (Fig. S12d) compared to CF300@Li. A rate capability test was carried out for the symmetrical cells using (Ni+ZnO)@Li or NF500@Li electrodes, whereas larger polarization was achieved for the cell using (Ni+ZnO)@Li electrodes (Fig. S12e). These results demonstrate the unique ability of the well dispersed Ni seeds in the Li composite electrodes for the improved bulk charge transfer, which cannot be achieved by the hetero-metal clusters derived from lithiophilic materials.

Based on the above results, the Ni-seeded Li electrodes are expected to provide improved performances for the cycling of Li metal at high DOD and low N/P ratio. To verify the latter, thinner Ni net (denoted as NN) was thermally treated at 500 °C to form NN500, which was used as the scaffold to fabricate a thin composite electrode (Fig. S13). As shown in Fig. S14a, the as-obtained NN500@Li electrode has a thick-

ness ~ 80 µm, and the Li loading is ~ 10 mAh cm^{-2} by measuring the electrode weights before/after Li infusion. By performing 5 cycles of Li plating/stripping in C-ELY, a very compact surface was maintained on NN500@Li (Fig. S14c), while a rough surface was already formed on a thin Li foil (~ 50 µm) with similar Li loading of 10 mAh cm^{-2} (Fig. S14b). Li||LiFePO$_4$ (LFP) full cells were employed to assess the stability of thin anodes, as shown in Fig. S14d and S14e. Based on the actual capacities of the anode (~ 10 mAh cm^{-2}) and LFP (~ 0.5 mAh cm^{-2}), a moderate N/P ratio of 20 is achieved, and the cell using NN500@Li anode showed clearly improved cycling stability over 450 cycles, outperforming that of the cell using 50 µm Li anode. It should be mentioned that the cell using NF500@Li anode with an N/P ratio of 130 could maintain a very stable long-term cycling over 600 cycles, demonstrating the use of excessive Li as a passive condition for achieving stable cycling of Li metal anode. These results indicate that further interfacial chemistry should be conjointly addressed to minimize the side reactions,
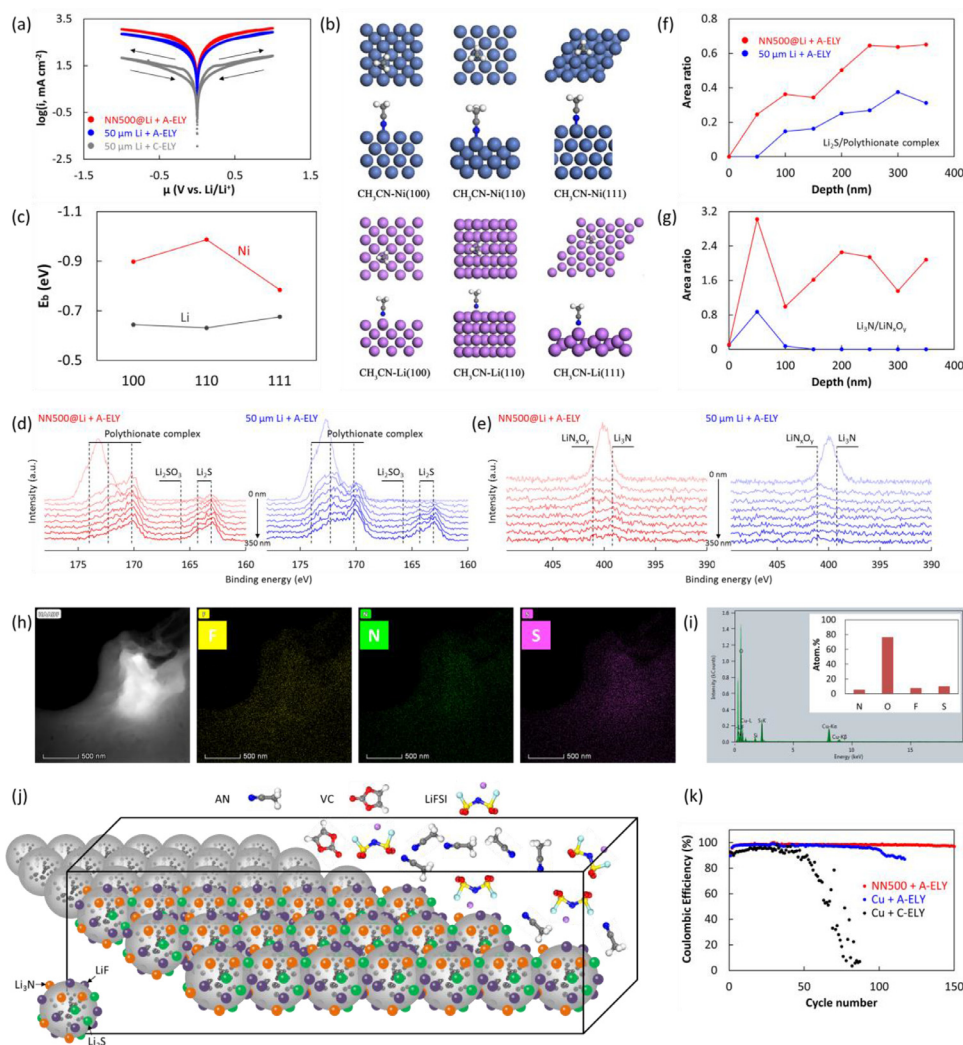
Fig. 4. (a) Tafel plots of symmetrical cells using 50 μm Li electrodes in C-ELY or A-ELY, and using NN500@Li electrodes in A-ELY; (b) AN molecule adsorptions on various facets of Ni and Li surfaces; (c) Binding energies of AN molecule on various facets of Ni and Li surfaces; (d, e) Ar$^+$-etching assisted XPS analysis, with (d) S 2p and (e) N 1 s spectra of the pre-cycled NN500@Li and 50 μm Li electrodes in A-ELY; (f, g) Area ratios of (f) Li$_2$S/Polythionate complex and (g) Li$_3$N/LiN$_x$O$_y$ at different depths of the pre-cycled NN500@Li and 50 μm Li electrodes in A-ELY; (h) EDS mapping and (i) related atomic percentages of F, N, S elements on the pre-cycled NN500@Li; (j) Schematic representation of the tailored interfacial chemistry in the bulk structure of Ni-seeded Li in A-ELY; (k) Cycling Li CEs on Cu in C-ELY or A-ELY, and on NN500 in A-ELY.

in addition to the deeply improved bulk charge transfer of the Ni-seeded Li electrode for stable LMBs at a low N/P ratio.

2.2. Synergism of nickel seeding and LiF-Li$_3$N-Li$_2$S co-doped interphase for Li metal cycling

The most efficient remedy to tailor the interfacial chemistry on the Li metal surface is based on the electrolyte formulation. It is well established that the reductions of conventional carbonate solvents not only result in chemically inhomogeneous and mechanically weak SEI layers mainly consisted of Li alkyl carbonate (ROCO$_2$Li) species, but also exhibit poor charge transfer kinetic at the Li/electrolyte interfaces [33]. In our previous work, an AN-based electrolyte (A-ELY) compatible with Li metal anodes was successively applied in high-power LMBs for the first time, leading to the high-quality SEI layer, low-surface-area Li deposits, and fast ion transfer as well as high Li CE at high current densities [34], however, its ability of stabilizing Li anode in conditions of low N/P ratio remains to be demonstrated. Thus, this A-ELY is employed in this work to assess its synergism with the Ni-seeded Li anodes. As shown in Fig. 4a, the Tafel plots obtained from potentiodynamic scanning of the symmetrical cells using 50 μm Li electrodes show first a significant increase of exchange current density using A-ELY, compared to that using C-ELY, demonstrating the significantly improved charge transfer in A-ELY. For the symmetrical cell using NN500@Li electrodes, a further increase of exchange current density was achieved compared to that of the cell using 50 μm Li, certifying the benefit of Ni seeding for accelerated Li$^+$

transfer, and the as-obtained exchange current density (419.1 mA cm^{-2}) is ∼ 20 times higher than that of bare Li in C-ELY (20.0 mA cm^{-2}).

Besides the higher binding energy of Li atoms on Ni seeds (Fig. 2c), another possible reason for the higher exchange current density of the cell using NN500@Li than that using 50 μm Li in A-ELY might be the stronger adsorption of electrolyte solvents on the Ni seeds, leading to a better transfer of the AN-solvated Li$^+$ ions through the bulk structure in NN500@Li. To address the latter assumption, adsorptions of AN molecule on various facets of Ni and Li surfaces were studied by computational modeling (Fig. 4b), and the as-calculated binding energies effectively reveal the better adsorptions of AN molecule on Ni surfaces than those on Li surfaces (Fig. 4c). These results not only explain the observed trend in exchange current densities, but also conduct to a tailored interfacial chemistry in the bulk structure of NN500@Li by the reactions with A-ELY. A systematic XPS analysis with Ar$^+$-etching process was carried out for pre-cycled NN500@Li and 50 μm Li (5 cycles Li plating/stripping of 4 mAh cm^{-2}). According to the fitting of F 1 s spectrum (Fig. S15a) and the evolution along the etched depths (Fig. S15b), LiF (684.8 eV) was revealed as the main F species in the NN500@Li electrode, which should arise from the reduction of LiFSI salt [34]. The presence of LiF with weaker signal was observed in the pre-cycled Li anode in A-ELY (Fig. S15b). Besides LiF, polythionate complex (170–175 eV), Li$_2$S (163–165 eV), LiN$_x$O$_y$ (401.1 eV) and Li$_3$N (399.2 eV) were also observed on these electrodes (Figs. S15a, 4d and 4e) [35,36]. Remarkably, more pronounced signals of Li$_2$S and Li$_3$N were observed for the pre-cycled NN500@Li electrode compared to the bare Li counterpart (Fig. 4d and

e), indicating a mediated surface chemistry on the Ni seeded Li anode. The area ratio of the relevant S 2p peaks (Li$_2$S/Polythionate complex, Fig. 4f) and N 1 s peaks (Li$_3$N/LiN$_x$O$_y$, Fig. 4g) clearly demonstrate the tailored interfacial chemistry in the Ni-seeded Li electrode with A-ELY. Furthermore, the uniform distributions of the F, N and S components in the bulk structure of NN500@Li were also demonstrated by the EDS mapping of high angle annular dark field-transmission electron microscope (HAADF-TEM) images (Fig. 4h), with relevant atomic percentages (Fig. 4i). Previously, the LiF-, Li$_3$N- or Li$_2$S-enriched Li interphases obtained via liquid or gaseous contact reactions were proved to provide high Li$^+$ ion diffusion rate to suppress dendrite growth and improve cycling stability of Li metal anode [37–42], which are also demonstrated in this work (Fig. S16a to S16c). Besides, the LiF-Li$_3$N-Li$_2$S co-doped Li interphase obtained by cycling with A-ELY could further improve the interfacial stability than those only enriched in LiF, Li$_3$N or Li$_2$S (Fig. S16d). Furthermore, this co-doped prominent interphase was uniformly generated and wrapped on the Ni-seeded structure, as schematically illustrated in Fig. 4j. Consistently, much improved Li cycling CEs could be achieved based on this optimal interfacial and bulk structure, with a high CE stabilized at ~99% for NN500 + A-ELY (Fig. 4k). The Li CE in A-ELY on bare Cu could also achieve a high value of ~99%, however, exhibiting shorter cycling life due to the lack of Ni seeding effect. In the case of Li cycling on bare Cu in C-ELY, much poorer CE of ~ 95% was obtained with a fluctuating cycling.

The impacts of Ni seeding and the tailored interfacial chemistry on Li plating/stripping morphologies were further studied, by performing various Li stripping-plating sequences (stripping of 4 mAh cm^{-2} Li, then plating-back of 1, 2 and 4 mAh cm^{-2} Li, denoted as states S4, S4-P1, S4-P2 and S4-P4, respectively) on 50 μm Li, NN@Li (Fig. 5a) and NN500@Li electrodes (Fig. 5f). The sample of NN@Li corresponds to a 50 μm Li foil mechanically pressed on a bare NN, with aims of differentiating the effect of Ni scaffold from that of the Ni seeds. The bulk structural difference between NN@Li and NN500@Li could be delicately probed by their XRD patterns with the peaks of Ni(111) and Li(111) (Fig. S17a), whereas a larger FWHM of Ni(111) peak was observed for the sample of NN500@Li (Fig. S17b), probably arising from the nano-crystals of Ni seeds imbedded in the composite electrode. The Li stripping of 4 mAh cm^{-2} represents a DOD of 40% for the investigated samples, leading to a drastic heterogeneous surface of NN@Li with uneven protuberances (Fig. 5b and c), depicting the difficulty of remaining uniform Li stripping process by only using 3D scaffold structures without a rational control of bulk charge transfer. In contrast, the scaffold of NN500@Li was uniformly covered by the residual Li layer at the state S4 (Fig. 5g and h), demonstrating the ability of Ni seeds to enhance the Li stripping process. For the Li plating-back sequences, highly porous structures were formed on NN@Li from states S4-P1 to S4-P4 (Fig. 5b), leaving tremendous void spaces (Fig. 5d and e). It should be mentioned that the Li deposits formed in A-ELY possess themselves suitable noodle-like shapes leading to lower surface-area contact and fewer side reactions with electrolyte (Fig. S18a), which outperform the dendritic deposits formed in C-ELY (Fig. 3a) [34]. However, the large noodle-like deposits could engender precipitations with each other, leading to the unoccupied void space and porous structure, on bare Li and NN@Li electrodes (Figs. 5b and S18b). Only in the case of NN500@Li, significantly enhanced morphologies during Li plating-back processes were achieved with the aid of Ni seeds (Fig. 5g), with progressive generations of compact Li deposits on preexisting nucleation sites (state S4-P1, Fig. 5i) and tangling with each other to form a compact Li surface (state S4-P4, Fig. 5j). It should be mentioned that the ultra-flat surface of NN500@Li at the state S4-P4 corresponds to a uniform SEI layer formed on the compact Li layer, which could be removed by extended exposure to electron beam (Fig. S19). Besides the morphologies, the stabilized structure and interphase for the Ni-seeded Li anode cycling with A-ELY were also verified by the electrochemical impedance spectroscopy (EIS) study at different depths of discharge (the states of S4, S4-P1, S4-P2 and S4-P4, Fig. S20). The uniform Li striping/plating on the NN500@Li elec-

trode in A-ELY could also be maintained for a high DOD of 80% (Fig. S21), indicating the possibility of deeply cyclable lithium metal anodes by the synergism of Ni seeding and LiF-Li$_3$N-Li$_2$S co-doped interphase. An overview of Li plating/stripping behaviors in the investigated samples in A-ELY are shown in Fig. 5k, whereas the remained uniform and compact structure in NN500@Li could be viewed as the consequence of synergism by Ni seeding and the LiF-Li$_3$N-Li$_2$S co-doped interphase.

The above results demonstrate the uniform Li stripping/plating at a high DOD of 40% on the NN500@Li electrode in A-ELY, showing the possibility of deeply cycling Li meal anode with a low N/P ratio. Thus, Li||LiNi$_{0.88}$Co$_{0.09}$Al$_{0.03}$O$_2$ (NCA) full cells were used as a proof-of-concept, whereas the capacities of anodes (10 mAh cm^{-2}) and cathodes (5 mAh cm^{-2}) conduct a low N/P ratio of 2. The performances of Li||NCA cells are shown in Fig. 6a. For the cells using 50 μm Li anodes, a large increase of CE was achieved by the cell using A-ELY (98.0%), compared to that using C-ELY (95.8%), demonstrating the better compatibility of A-ELY with Li anodes. However, this improvement is still insufficient to enable long-term cycling of LMBs at low N/P ratio, as shown by the serious capacity fading beyond the 100th cycle. As well, the single use of NN@Li anode without Ni seeding could not significantly improve the cycling performances, and a radical capacity fading occurred after 80 cycles, leading to a low average CE of 96.4%. This feature indicates that only reinforcing the Li anode by a single 3D scaffold could not improve the bulk charge transfer of Li metal anode for deep Li plating/stripping. Only for the cell using NN500@Li anode and A-ELY, stable cycling over 160 cycles was achieved with a high average CE of 99.6%, demonstrating the beneficial effect of Ni seeding for deep Li metal cycling.

The latter feature could be further illustrated by the evolution of dQ/dV profiles derived from the charge/discharge curves between the 1st and 100th cycles (Fig. 6b to e). For the cell using 50 μm Li anode and C-ELY, the peak intensities decrease dramatically between the 1st and 100th cycles (Fig. 6b), implying the fast increase of polarization caused by the consumption of active Li and seriously deteriorated electrode structures. Remarkably, for the cells using A-ELY, the dQ/dV profiles of the cell using NN500@Li anode nearly maintain the shape over 100 cycles (Fig. 6e), exhibiting much higher stability than those of the cells using 50 μm Li or NN@Li anodes (Fig. 6c and d, respectively). The morphologies of the cycled 50 μm Li in C-ELY and A-ELY, and NN500@Li in A-ELY after 50 cycles were also measured. As shown in Fig. S22, the cycled 50 μm Li in A-ELY exhibits a more compact surface than that of the cycled 50 μm Li in C-ELY. The amplified image shows the noodle-like Li deposits on the cycled 50 μm Li in A-ELY, while highly pulverized surface is observed for the cycled 50 μm Li in C-ELY. Despite the improved Li deposition in A-ELY, surface cracks were still observed for the cycled 50 μm Li. In contrast, an intact surface was obtained for the cycled NN500@Li in A-ELY. These results indicate the much improved charge transfer of Li anode by the synergetic effect of Ni seeding and LiF-Li$_3$N-Li$_2$S co-doped interphase.

It should be mentioned that the above Ni seeded Li anode was derived from the NN500, which is not slight due to the weight of Ni skeleton. To further boost the energy density of the LMBs, a slight carbon net (CN, Fig. 6f) was used to fabricate the NiO decorated scaffold, which was then subject to fabricate Ni seeded Li anode in molten Li. This NiO decorated CN was obtained by heating a CN precursor at 400 °C, and will be denoted as CN400 afterwards. As shown in Fig. 6g, a NiO coating was successively realized on CN400. Furthermore, the Ni seeded structure could be clearly observed in the cross-sectional SEM image of CN400@Li (Fig. 6h). Based on the slight CN400@Li anode, a pie chart of the weight distributions of all cell components is given in Fig. 6i and Table S1, and an energy density of 351.2 Wh kg^{-1} was achieved for the Li||NCA cell (Fig. 6j). It should be mentioned that this energy density was calculated based on the geometry of a 2032 coin cell, while the value could be further raised in pouch cell design. The cycling stability of the Li||NCA cell using CN400@Li anode is shown in Fig. S23, stable cycling with an average CE of 99.0% over 100 cycles is achieved, which is close
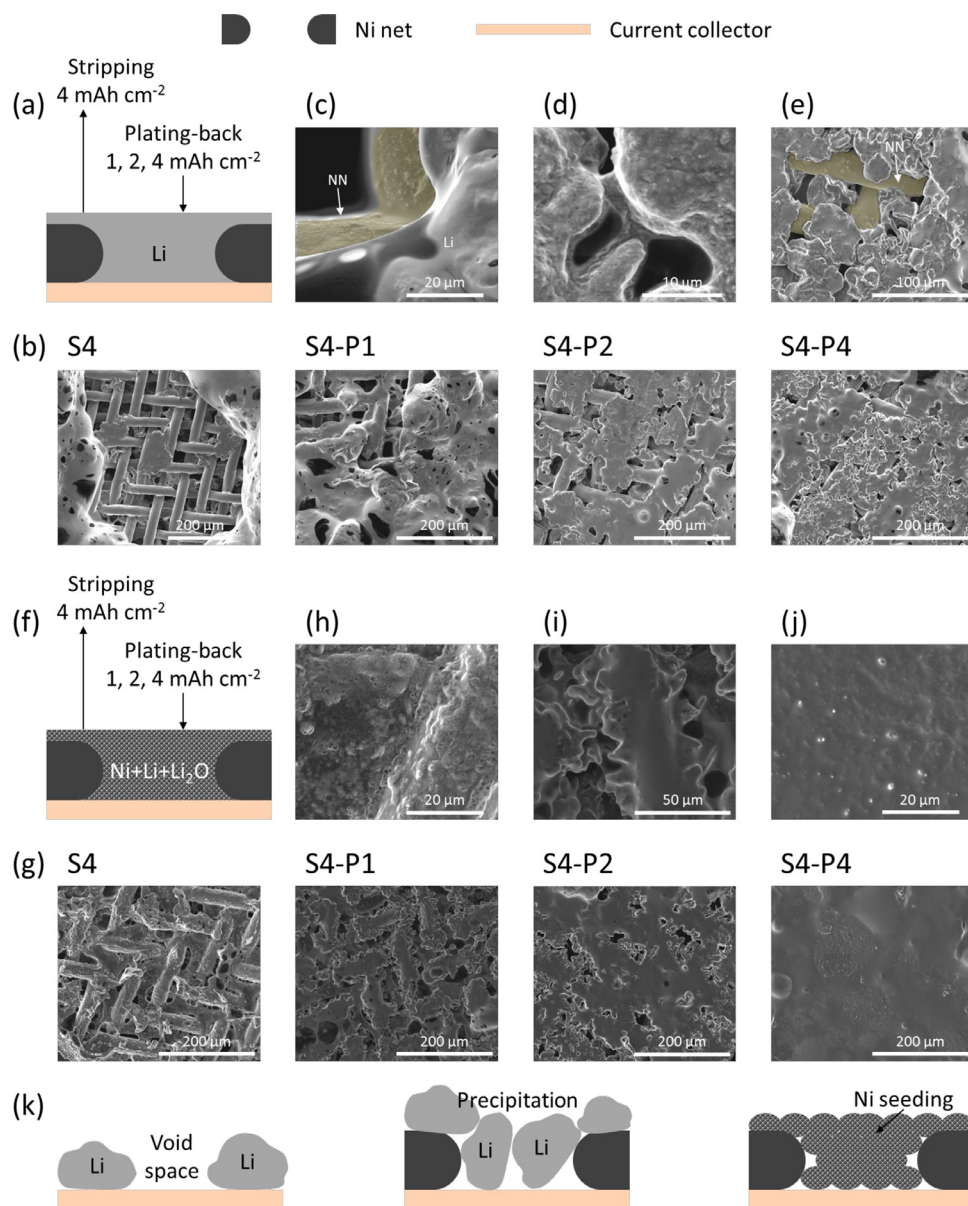
Fig. 5. (a) Schematic representation of Li plating/stripping sequences on NN@Li; (b) Morphologies of NN@Li electrodes following various Li plating/stripping sequences in A-ELY; (c-e) Amplified morphologies of NN@Li electrodes at the states (c) S4, (d) S4-P1 and (e) S4-P4; (f) Schematic representation of Li plating/stripping sequences on NN500@Li; (g) Morphologies of NN500@Li electrodes following various Li plating/stripping sequences in A-ELY; (h-j) Amplified morphologies of NN500@Li electrodes at the states (h) S4, (i) S4-P1 and (j) S4-P4; (k) Schematic representations of Li plating-back behaviors on 50 μm Li, NN@Li and NN500@Li electrodes in A-ELY.

to the cell using NN500@Li anode. However, fluctuating performances were obtained beyond 100 cycles for the cell using CN400@Li anode, and one possible reason is the structure collapse of the CN400 scaffold which became fragile after the heating process. These results indicate the need for further structural optimization of the slight NiO coated carbon structures, which should be highly feasible regarding the quickly developed innovative technology for nanostructured carbon productions. However, the present results already form a good database to demonstrate the synergism of Ni seeding and tailored interfacial chemistry for deeply improved bulk charge transfer of Li metal anodes.

3. Conclusions

To stabilize the cycling of Li metal anode at a low N/P ratio, which is a prerequisite for achieving high-energy-density LMBs, the multiple protective strategies were investigated, via the synergism of Ni seeding and tailored interfacial chemistry. The highly lithiophilic NiO coated structures and negligible solubility of Ni in molten Li leaded to the facile fabrication of Ni seeded Li anodes. The Ni seeds in the bulk Li anode not only provided high binding energy with Li atoms and acted as the

well-dispersed Li nucleation sites for the Ni-seeded growth of granular Li deposits, but also enabled the formation a fast Li^+ conducting interphase with co-produced LiF, Li_3N and Li_2S components when deeply cycling with an acetonitrile-based electrolyte, leading to an exchange current density $\sim$ 20 times higher than that of bare Li in conventional carbonate electrolytes, and uniform Li plating/striping in deep cycling conditions at a high DOD of 40%. Consequently, stable cycling of LMBs with high-loading cathodes ($\sim$ 5 mAh cm^{-2}) at the low N/P capacity ratio of 2 was achieved, and proof-of-concept high-energy-density LMBs (> 350 Wh kg^{-1}) was also demonstrated. These results shed new light on the designing of thin and stable Li metal anodes for high-energy-density LMBs.

4. Experimental section

4.1. Material preparations

To prepare the metal oxide coated structures, Cu form (CF), Ni form (NF) or Ni net (NN) were heated in an air-filled muffle furnace, with a heating rate of 10 °C min^{-1} up to the desired temperature fol-
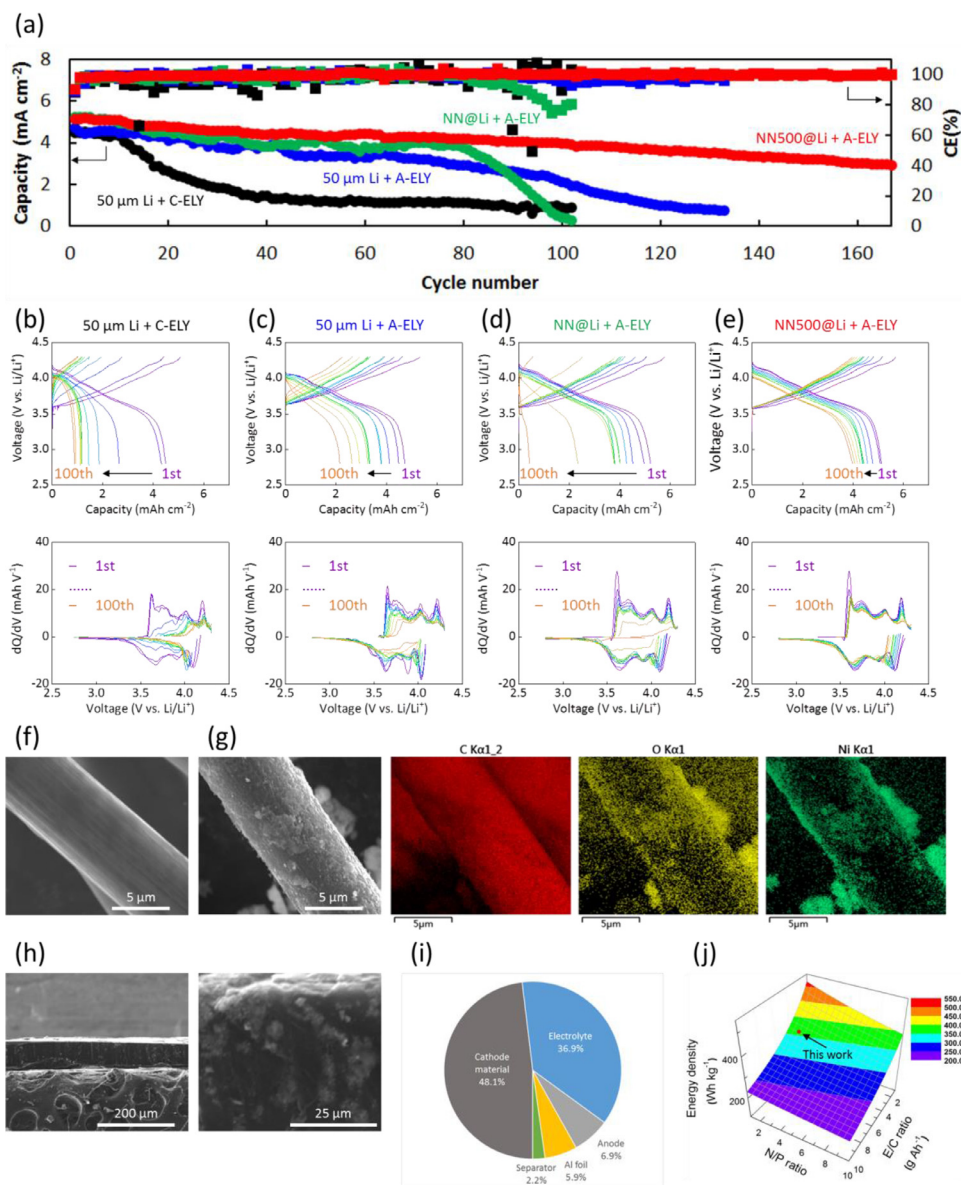
Fig. 6. (a) Cycling performances of Li||NCA full cells using various anodes and electrolytes; (b-e) Charge-discharge curves and related dQ/dV profiles of Li||NCA full cells using (b) 50 μm Li anode and C-ELY, (c) 50 μm Li anode and A-ELY, (d) NN@Li anode and A-ELY and (e) NN500@Li anode and A-ELY; (f) SEM image of pristine CN; (g) SEM and EDS images of CN400; (h) Cross-sectional SEM images of CN400@Li; (i) A pie chart of the weight distributions of all cell components and (j) energy density of Li||NCA full cell using CN400@Li anode.

lowed by maintaining the temperature for 0.5 h. The NiO coated carbon net (CN) was obtained via a hydrothermal process. Briefly, 2.38 g $Ni(NO_3)_2 \cdot 6H_2O$ and 0.3 g urea were dissolved in 20 mL deionized water, followed by immersing a foil of CN. This mixture was put in a 100 mL autoclave, which was then sealed and maintained at 90 °C for 12 h. The as-obtained CN was rinsed with deionized water, dried at 60 °C for 1 h, and finally heated in the air-filled muffle furnace with a heating rate of 5 °C min⁻¹ up to 400 °C then maintained for 2 h. The composite electrodes (CF300@Li, NF500@Li, NN500@Li and CN400@Li) were obtained by immersion of the metal oxide coated structures into molten Li at 250 °C.

4.2. Electrochemical measurements

$LiPF_6$, ethylene carbonate (EC), diethyl carbonate (DEC), fluoroethylene carbonate (FEC), and vinylene carbonate (VC) were purchased from Alfa Aesar. Lithium Bis(fluorosulfonyl)imide (LiFSI) and acetonitrile (AN) was purchased from Aladdin. The carbonate-based electrolyte consists of 1 M $LiPF_6$ in EC:DEC (1:1 by vol.) with 5 vol% FEC, and the AN-based electrolyte consists of 10 M LiFSI in AN with 10 vol% VC. Coin cells CR2032 were used for cell assembly, with Celgard separator

films 2320 and 3501 for the carbonate-base and AN-based electrolytes, respectively.

For cycling tests of Li||Cu cells, Li foil was used as counter and reference electrodes, and Cu foil, CF300, NF500, or NN500 was used as working electrode. Li plating was performed at 0.5 mA cm⁻² for an areal capacity of 1 mAh cm⁻², followed by Li stripping up to a cut-off potential to 1 V vs. Li/Li⁺. Cycling tests of symmetrical cells using Li foil, CF300@Li or NF500@Li electrodes were carried out at a current density of 0.5 mA cm⁻² for a fixed capacity of 1 mAh cm⁻². All the cycling tests were carried out using Land BT2000 battery testers. The Tafel plots and EIS of symmetrical cells were obtained using a potentiostat/galvanostat 1470E from Solartron. The EIS measurements were performed in the frequency range from 1×10^5 to 1×10^{-1} Hz with a voltage perturbation of 5 mV.

For cycling tests of Li||LiFePO₄ (LFP) full cells, the LFP cathodes were obtained by casting the slurry of LFP:Super-P:PVDF (8:1:1, w/w/w) on Al foils, followed by vacuum drying at 120 °C for 12 h. The areal loading of LFP cathodes is ~0.5 mAh cm⁻² (160 mAh g⁻¹ of active LFP material). The Li||LFP cells were pre-cycled for three cycles at charge/discharge rates of 0.1C/0.1C in a voltage window of 2.5–4.4 V vs. Li/Li⁺, followed by cycling at 0.5C/0.5C. For

Li‖LiNi$_{0.88}$Co$_{0.09}$Al$_{0.03}$O$_2$ (NCA) full cells, thick NCA electrodes with a high areal capacity loading of ~5 mAh cm^{-2} were provided by CEC New Energy (Wuhan) Research Institute Co., LTD. All the Li‖NCA cells were pre-cycled for three cycles at charge/discharge rates of 0.1C/0.1C in a voltage window of 2.8–4.3 V vs. Li/Li$^+$, followed by cycling at 0.1C/0.3C.

4.3. Electrodes characterizations

Surface morphology and elemental mapping were performed using SEM (FEI, QUANTA 250 FEG). The high-resolution images and elemental mapping were obtained using TEM (Talos F200X, 200 kV). Surface chemistry analysis was conducted with a PHI 3056 XPS, which was excited by a Mg Kα radiation source at a constant power of 100 W (15 kV and 6.67 mA). The crystalline phase of the prepared samples was characterized by XRD with a Bruker D8 advanced diffractometer using Cu Kα (λ = 1.5406 Å) radiation (Bruker axs, D8 Advance).

4.4. Computational details

Periodic density functional theory (DFT) calculations were performed by using the Vienna ab initio simulation package (VASP) code [43,44]. The electron–ion interactions were calculated by the projected augmented wave (PAW) method [45,46], and the exchange–correlation energies were described by the generalized gradient approximation (GGA) with the Perdew-Burke-Ernzerhof (PBE) functional [47]. The Cu(100), Ni(100), Ni(111), Li(100), Li(111) surfaces were built by 3×3 unit cells, Li(110) and Ni(110) were built by 3×2 and 2×3 unit cells, respectively. All surfaces are four periodic atom layers and the vacuum thickness was 10 Å to remove any interactions between slabs. The bottom two layers were fixed and the top two layers were fully relaxed. The cutoff energy was 400 eV and the calculations were stopped when forces on all atoms were less than 0.05 eV $Å^{-1}$. The Brillouin zone sampling was carried out using Monkhorst-Pack k-points of $4 \times 4 \times 1$. The adsorption energy (E$_{ads}$) was calculated according to the following equation:

$$E_{ads} = E_{surface\text{-}adsorbate} - E_{surface} - E_{adsorbate}$$

where E$_{surf\text{-}adsorbate}$, E$_{surface}$ and E$_{adsorbate}$ are the energies of the adsorbed system, the clean surface and the free adsorbate in gas phase, respectively.

Credit author statement

Zhendong Li: Conceptualization, Methodology, Software, Data curation, Investigation, Writing-original draft preparation, Validation;
Liyuan Huai: Computational implementation;
Shun Li: Data analysis of the optimal images;
Mingming Ma: Data analysis of the XPS results;
Kailin Luo: Battery testing;
Yang Zhao: Discussion, Writing-Review & Editing;
Deyu Wang: Supervision, Writing-Review & Editing, Funding acquisition;
Xueliang Sun: Supervision, Writing-Review & Editing;
Zhe Peng: Conceptualization, Supervision, Writing-Review & Editing, Funding acquisition.

Declaration of Competing Interest

The authors declare that they have no known competing financial interests or personal relationships that could have appeared to influence the work reported in this paper.

Acknowledgments

Supplementary materials

References

[1] M. Armand, J.M. Tarascon, Building better batteries, Nature 451 (2008) 652–657.
[2] J.B. Goodenough, Energy storage materials: a perspective, Energy Storage Mater. 1 (2015) 158–161.
[3] P.G. Bruce, S.A. Freunberger, L.J. Hardwick, J.-.M. Tarascon, Li-O$_2$ and Li-S batteries with high energy storage, Nat. Mater. 11 (2012) 19–29.
[4] X.-.B. Cheng, R. Zhang, C.-.Z. Zhao, Q. Zhang, Toward safe lithium metal anode in rechargeable batteries: a review, Chem. Rev. 117 (2017) 10403–10473.
[5] S.T. Boles, M.H. Tahmasebi, Are foils the future of anodes? Joule (2020), doi:10.1016/j.joule.2020.05.009.
[6] J.-.G. Zhang, Anode-less, Nat. Energy 4 (2019) 637–638.
[7] W. Xu, J. Wang, F. Ding, X. Chen, E. Nasybulin, Y. Zhang, J.-.G. Zhang, Lithium metal anodes for rechargeable batteries, Energy Environ. Sci. 7 (2014) 513–537.
[8] X.-.Q. Zhang, X.-.B. Cheng, X. Chen, C. Yan, Q. Zhang, Fluoroethylene carbonate additives to render uniform Li deposits in lithium metal batteries, Adv. Funct. Mater. 27 (2017) 1605989.
[9] E. Markevich, G. Salitra, F. Chesneau, M. Schmidt, D. Aurbach, Very stable lithium metal stripping-plating at a high rate and high areal capacity in fluoroethylene carbonate-based organic electrolyte solution, ACS Energy Lett 2 (2017) 1321–1326.
[10] X. Li, J. Zheng, X. Ren, M.H. Engelhard, W. Zhao, Q. Li, J.-.G. Zhang, W. Xu, Dendrite-free and performance-enhanced lithium metal batteries through optimizing solvent compositions and adding combinational additives, Adv. Energy Mater. 8 (2018) 1703022.
[11] H. Yu, J. Zhao, L. Ben, Y. Zhan, Y. Wu, X. Huang, Dendrite-free lithium deposition with self-aligned columnar structure in a carbonate-ether mixed electrolyte, ACS Energy Lett. 2 (2017) 1296–1302.
[12] W. Zhou, S. Wang, Y. Li, S. Xin, A. Manthiram, J.B. Goodenough, Plating a dendrite-free lithium anode with a polymer/ceramic/polymer sandwich electrolyte, J. Am. Chem. Soc. 138 (2016) 9385–9388.
[13] C. Yan, X.-.B. Cheng, Y.-.X. Yao, X. Shen, B.-.Q. Li, W.-.J. Li, R. Zhang, J.-.Q. Huang, H. Li, Q. Zhang, An armored mixed conductor interphase on a dendrite-free lithium-metal anode, Adv. Mater. 30 (2018) 1804461.
[14] X. Liang, Q. Pang, I.R. Kochetkov, M.S. Sempere, H. Huang, X. Sun, L.F. Nazar, A facile surface chemistry route to a stabilized lithium metal anode, Nat. Energy 2 (2017) 17119.
[15] E. Cha, M.D. Patel, J. Park, J. Hwang, V. Prasad, K. Cho, W. Choi, 2D MoS$_2$ as an efficient protective layer for lithium metal anodes in high-performance Li-S batteries, Nat. Nanotechnol. 13 (2018) 337–344.
[16] Z. Tu, S. Choudhury, M.J. Zachman, S. Wei, K. Zhang, L.F. Kourkoutis, L.A. Archer, Fast ion transport at solid-solid interfaces in hybrid battery anodes, Nat. Energy 3 (2018) 310–316.
[17] L.-.L. Lu, J. Ge, J.-.N. Yang, S.-.M. Chen, H.-.B. Yao, F. Zhou, S.-.H. Yu, Free-standing copper nanowire network current collector for improving lithium anode performance, Nano Lett. 16 (2016) 4431–4437.
[18] H. Ye, S. Xin, Y.-.X. Yin, J.-.Y. Li, Y.-.G. Guo, L.-.J. Wan, Stable Li plating/stripping electrochemistry realized by a hybrid Li reservoir in spherical carbon granules with 3D conducting skeletons, J. Am. Chem. Soc. 139 (2017) 5916–5922.
[19] T.-.T. Zuo, X.-.W. Wu, C.-.P. Yang, Y.-.X. Yin, H. Ye, N.-.W. Li, Y.-.G. Guo, Graphitized carbon fibers as multifunctional 3D current collectors for high areal capacity Li anodes, Adv. Mater. 29 (2017) 1700389.
[20] C. Yang, Y. Yao, S. He, H. Xie, E. Hitz, L. Hu, Ultrafine silver nanoparticles for seeded lithium deposition toward stable lithium metal anode, Adv. Mater. 29 (2017) 1702714.
[21] R. Zhang, X. Chen, X. Shen, X.-.Q. Zhang, X.-.R. Chen, X.-.B. Cheng, C. Yan, C.-.Z. Zhao, Q. Zhang, Coralloid carbon fiber-based composite lithium anode for robust lithium metal batteries, Joule 2 (2018) 764–777.
[22] M.S. Kim, J.-.H. Ryu, Y.R.Lim Deepika, I.W. Nah, K.-.R. Lee, L.A. Archer, W.I. Cho, Langmuir–Blodgett artificial solid-electrolyte interphases for practical lithium metal batteries, Nat. Energy 3 (2018) 889–898.
[23] C. Niu, H. Lee, S. Chen, Q. Li, J. Du, W. Xu, J.-.G. Zhang, M.S. Whittingham, J. Xiao, J. Liu, High-energy lithium metal pouch cells with limited anode swelling and long stable cycles, Nat. Energy 4 (2019) 551–559.
[24] P. Shi, X.-.B. Cheng, T. Li, R. Zhang, H. Liu, C. Yan, X.-.Q. Zhang, J.-.Q. Huang, Q. Zhang, Electrochemical diagram of an ultrathin lithium metal anode in pouch cells, Adv. Mater. 31 (2019) 1902785.
[25] Y. Gao, M. Guo, K. Yuan, C. Shen, Z. Ren, K. Zhang, H. Zhao, F. Qiao, J. Gu, Y. Qi, K. Xie, B. Wei, Multifunctional silanization interface for high-energy and low-gassing lithium metal pouch cells, Adv. Energy Mater. 10 (2020) 1903362.
[26] Z. Zhang, Z. Xu, S. Wang, Z. Peng, M. Liu, J. Zhou, C. Shen, D. Wang, Li$_2$O-reinforced Cu nanoclusters as porous structure for dendrite-free and long-lifespan lithium metal anode, ACS Appl. Mater. Interfaces 8 (2016) 26801–26808.
[27] X.-.Y. Yue, X.-.L. Li, W.-.W. Wang, D. Chen, Q.-.Q. Qiu, Q.-.C. Wang, X.-.J. Wu, Z.-.W. Fu, Z. Shadike, X.-.Q. Yang, Y.-.N. Zhou, Wettable carbon felt framework for high loading Li-metal composite anode, Nano Energy 60 (2019) 257–266.
[28] M. Wang, Z. Peng, W. Luo, Q. Zhang, Z. Li, Y. Zhu, H. Lin, L. Cai, X. Yao, C. Ouyang, D. Wang, Improving the interfacial stability between lithium and solid-state electrolyte via dipole-structured lithium layer deposited on graphene oxide, Adv. Sci. 7 (2020) 2000237.

[29] J. Zheng, M.H. Engelhard, D. Mei, S. Jiao, B.J. Polzin, J.-.G. Zhang, W. Xu, Electrolyte additive enabled fast charging and stable cycling lithium metal batteries, Nat. Energy 2 (2017) 17012.

[30] T.B. Massalski, H. Okamoto, Binary Alloy Phase Diagrams, ASM International, 1990.

[31] J. Jia, Z. Tang, Z. Guo, H. Xu, H. Hu, S. Li, A 3D composite lithium metal anode with pre-fabricated LiZn via reactive wetting, Chem. Commun. 56 (2020) 4248–4251.

[32] J.H. Zheng, Q. Jiang, J.S. Lian, Synthesis and optical properties of flower-like ZnO nanorods by thermal evaporation method, Appl. Surf. Sci. 257 (2011) 5083–5087.

[33] F. Ding, W. Xu, X. Chen, J. Zhang, M.H. Engelhard, Y. Zhang, B.R. Johnson, J.V. Crum, T.A. Blake, X. Liu, J.-.G. Zhang, Effects of carbonate solvents and lithium salts on morphology and coulombic efficiency of lithium electrode, J. Electrochem. Soc. 160 (2013) A1894–A1901.

[34] Z. Peng, X. Cao, P. Gao, H. Jia, X. Ren, S. Roy, Z. Li, Y. Zhu, W. Xie, D. Liu, Q. Li, D. Wang, W. Xu, J.-.G. Zhang, High-power lithium metal batteries enabled by high–concentration acetonitrile-based electrolytes with vinylene carbonate additive, Adv. Funct. Mater. 30 (2020) 2001285.

[35] C.-.Z. Zhao, X.-.B. Cheng, R. Zhang, H.-.J. Peng, J.-.Q. Huang, R. Ran, Z.-.H. Huang, F. Wei, Q. Zhang, Li_2S_5-based ternary-salt electrolyte for robust lithium metal anode, Energy Storage Mater. 3 (2016) 77–84.

[36] X.-.B. Cheng, C. Yan, X. Chen, C. Guan, J.-.Q. Huang, H.-.J. Peng, R. Zhang, S.-.T. Yang, Q. Zhang, Implantable Solid Electrolyte Interphase in Lithium-Metal Batteries, Chem 2 (2017) 258–270.

[37] M. Wu, Z. Wen, Y. Liu, X. Wang, L. Huang, Electrochemical behaviors of a Li_3N modified Li metal electrode in secondary lithium batteries, J. Power Source 196 (2011) 8091–8097.

[38] G. Ma, Z. Wen, M. Wu, C. Shen, Q. Wang, J. Jin, X. Wu, A lithium anode protection guided highly-stable lithium-sulfur battery, Chem. Commun. 50 (2014) 14209–14212.

[39] D. Lin, Y. Liu, W. Chen, G. Zhou, K. Liu, B. Dunn, Y. Cui, Conformal lithium fluoride protection layer on three-dimensional lithium by nonhazardous gaseous reagent Freon, Nano Lett. 17 (2017) 3731–3737.

[40] Z. Peng, N. Zhao, Z. Zhang, H. Wan, H. Lin, M. Liu, C. Shen, H. He, X. Guo, J.-.G. Zhang, D. Wang, Stabilizing Li/electrolyte interface with a transplantable protective layer based on nanoscale LiF domains, Nano Energy 39 (2017) 662–672.

[41] F. Liu, L. Wang, Z. Zhang, P. Shi, Y. Feng, Y. Yao, S. Ye, H. Wang, X. Wu, Y. Yu, A mixed lithium-ion conductive Li_2S/Li_2Se protection layer for stable lithium metal anode, Adv. Funct. Mater. 30 (2020) 2001607.

[42] H. Chen, A. Pei, D. Lin, J. Xie, A. Yang, J. Xu, K. Lin, J. Wang, H. Wang, F. Shi, D. Boyle, Y. Cui, Uniform high ionic conducting lithium sulfide protection layer for stable lithium metal anode, Adv. Energy Mater. 9 (2019) 1900858.

[43] G. Kresse, J. Hafner, Ab initio, Ab initio molecular dynamics for liquid metals, Phys. Rev. B 47 (1993) 558–561.

[44] G. Kresse, J. Furthmüller, Efficient iterative schemes for ab initio total-energy calculations using a plane-wave basis set, Phys. Rev. B 54 (1996) 11169–11186.

[45] P.E. Blöchl, Projector augmented-wave method, Phys. Rev. B 50 (1994) 17953–17979.

[46] G. Kresse, D. Joubert, From ultrasoft pseudopotentials to the projector augmented-wave method, Phys. Rev. B 59 (1999) 1758–1775.

[47] J.P. Perdew, K. Burke, M. Ernzerhof, Generalized gradient approximation made simple, Phys. Rev. Lett. 77 (1996) 3865–3868.